Mantle to surface degassing of carbon- and sulphur-rich alkaline magma at El Hierro, Canary Islands

Marc-Antoine Longpré[1,2*], John Stix[3], Andreas Klügel[4], Nobumichi Shimizu[5]

[1]School of Earth and Environmental Sciences, Queens College, City University of New York, Queens, New York 11367, USA
[2]The Graduate Center, City University of New York, New York, New York 10016, USA
[3]Earth and Planetary Sciences, McGill University, Montréal, Québec, H3A 0E8, Canada
[4]Fachbereich Geowissenschaften, Universität Bremen, 28334 Bremen, Germany
[5]Woods Hole Oceanographic Institution, Woods Hole, Massachusetts 02543, USA
[*]*Corresponding author. Tel.: +1 718 997 3259. E-mail: mlongpre@qc.cuny.edu*

Abstract

Basaltic volcanoes transfer volatiles from the mantle to the surface of the Earth. The quantification of deep volatile fluxes relies heavily on estimates of the volatile content of primitive magmas, the best archive of which is provided by melt inclusions. Available data from volcanoes producing mafic alkaline lavas in a range of tectonic settings suggest high volatile fluxes, but information remains sparse, particularly for intraplate ocean islands. Here we present measurements of volatile and trace element concentrations, as well as sulphur speciation, in olivine-hosted melt inclusions and matrix glasses from quenched basanite lava balloon samples from the 2011–2012 submarine eruption at El Hierro, Canary Islands. The results reveal remarkably high concentrations of dissolved volatiles and incompatible trace elements in this magma, with ~80 ppm Nb and up to 3420 ppm CO_2, 3.0 wt% H_2O and 5080 ppm S. Reconstructed primitive CO_2 contents, considering CO_2/Nb systematics and possible CO_2 sequestration in shrinkage bubbles, reach weight percent levels, indicating that carbon is a major constituent of Canary Island magmas at depth and that exsolution of a CO_2-rich fluid begins in the mantle at pressures in excess of 1 GPa. Correlations between sulphur concentration, sulphur speciation and water content suggest strong reduction of an initially oxidised mantle magma, likely controlled by coupled H_2O and S degassing. This late-stage redox change may have triggered sulphide saturation, recorded by globular sulphide inclusions in clinopyroxene and ulvöspinel. The El Hierro basanite thus had a particularly high volatile-carrying capacity and released a minimum of 1.3–2.1 Tg CO_2 and 1.8–2.9 Tg S to the environment, causing substantial stress on the local submarine ecosystem. These results highlight the important contribution of alkaline ocean island volcanoes, such as the Canary Islands, to volatile fluxes from the mantle.

Keywords

Melt inclusion; carbon dioxide; sulfur; sulfide; degassing; Canary Islands

1. Introduction

Magma degassing of volatile compounds (CO_2, H_2O, S, F, Cl) is central to numerous Earth science problems, ranging from explosive volcanic eruptions, to ore-forming processes, and atmospheric chemistry and climate change. Deep CO_2 emissions from volcanoes, for example, are a poorly constrained, yet crucial input for modelling the long-term carbon cycle (Kelemen and Manning, 2015). Sulphur, in turn, with its multiple valences in silicate melts and volcanic gases, participates in key redox reactions in the mantle and atmosphere (Wallace and Edmonds, 2011). Quantifying fluxes of deep volatiles towards the surface requires estimates of their primary concentrations in basaltic magmas (including alkaline varieties) erupted at mid-ocean ridges, subduction zones and intraplate hotspots. During partial melting of the mantle, volatiles behave like other incompatible elements and are strongly concentrated in the melt phase (Saal et al., 2002). However, because the solubility of volatiles in silicate melts is primarily a function of pressure, erupted magmas typically do not preserve primary melt volatile contents — especially CO_2, H_2O and S — due to strong degassing upon ascent-driven decompression. To circumvent this problem, researchers turn to melt inclusions, which represent droplets of silicate melt trapped during crystal growth at depth. Protected by their mineral host acting as a pressure vessel, melt inclusions can retain volatiles during decompression and, assuming that any post-entrapment modification of their composition can be assessed, provide unique information on the degassing histories and original concentrations of volatiles in magmas (Métrich and Wallace, 2008).

Alkaline volcanism, in a range of tectonic settings, produces SiO_2-undersaturated magmas typically enriched in incompatible trace elements, reflecting low degrees of partial melting of possibly enriched mantle sources (e.g., McKenzie and O'Nions, 1991). Available melt inclusion data indicate that mafic alkaline magmas are volatile-rich (Hudgins et al., 2015; Oppenheimer et al., 2011; Spilliaert et al., 2006) and oxidised (Jugo et al., 2010; Métrich et al., 2009; Métrich and Clocchiatti, 1996; Moussallam et al., 2014), consistent with experimental evidence (e.g., Dixon, 1997; Lesne et al., 2011; Shishkina et al., 2014). This suggests that alkaline volcanoes, despite relatively modest magma output rates, may contribute significantly to deep volatile fluxes (e.g., Oppenheimer et al., 2011), but data remain sparse, particularly in intraplate oceanic settings.

The Canary Islands are a voluminous group of intraplate ocean island volcanoes that dominantly erupt alkaline magmas derived from a heterogeneous, deep (≥ 60–100 km) mantle source (e.g., Day et al., 2010; Gurenko et al., 2006; Sigmarsson et al., 1998). Information pertaining to the volatile budget of Canary Island magmas is scarce. Wallace (1998) reported CO_2 and H_2O concentrations reaching 1430 ppm and 1.4 wt%, respectively, in melt inclusions from basaltic hyaloclastites from the submarine flanks of Gran Canaria. Gurenko and Schmincke (2000) studied

similar samples and observed high S concentrations reaching 5800 ppm, of which up to 95% was found to be dissolved as sulphate. Abundant data on fluid inclusions exist, however, and attest to the presence of pervasive CO_2-rich fluids in the mantle beneath the Canaries (e.g., Hansteen et al., 1991; Hansteen et al., 1998).

From October 2011 to March 2012, a submarine eruption occurred about 2 km south of El Hierro, the westernmost and youngest island of the archipelago (Fig. 1) (see Carracedo et al., 2015 for a review). The eruption produced peculiar lava balloons (e.g., Kelly et al., 2014) that were collected while floating and degassing at the sea surface above the vent. Petrological and geophysical data indicate that mantle-derived basanite magma intruded the lower crust, where it migrated subhorizontally for ~15 km, and then rapidly transited to the surface, all within a few months (Longpré et al., 2014; Martí et al., 2013; Meletlidis et al., 2015).

In this paper, we present volatile and trace element concentrations, as well as sulphur speciation measurements, in olivine-hosted melt inclusions and their host matrix glasses from the El Hierro lava balloons. This represents the first comprehensive effort to constrain the degassing behaviour and volatile fluxes at Canary Island volcanoes. The results reveal the strong degassing and associated redox change of the initially volatile-rich and oxidised 2011–2012 magma as it ascended from the mantle to produce a Strombolian-type submarine eruption. Our findings also add to a growing body of evidence of high volatile outputs at alkaline volcanoes.

2. Samples and Methods

The quenched lava balloon fragments studied here were erupted at 100–300 m water depth and collected on 31 October, 27 November, and 6 December 2011, as well as 28 January 2012. We also analysed the matrix glass composition of the essentially aphyric basanitic crust of a bicoloured sample erupted on 15 October 2011, representing the minor, earliest eruptive products (e.g., Troll et al., 2012). Detailed petrologic investigations of the lava balloon samples were previously presented by Martí et al. (2013), Longpré et al. (2014), and Meletlidis et al. (2015). In brief, the lava contains phenocrysts of olivine, clinopyroxene, ulvöspinel and rare ilmenite that are set in a glassy matrix containing microlites of the same minerals, in addition to minor plagioclase. Phenocrysts host inclusions of Fe-Ti oxides, glass (melt inclusions) and CO_2-rich fluid. Notably, large (up to 200 µm across) globular sulphides also frequently occur as inclusions in clinopyroxene and ulvöspinel, often near or on the rims of crystals (Fig. 2c), but not in olivine nor as a free phase in matrix glass. This work focuses on melt inclusions (20–150 µm) in olivine, virtually all of which feature vapour bubbles occupying 5 ± 2 % of the inclusion volume (Fig. 2). Some melt inclusions also contain microlites, most commonly Fe-Ti oxide, tiny (0.1 ± 0.1 vol%, i.e. ≤ 5 µm) sulphide spheres and clinopyroxene (Fig. 2).

We generally targeted glassy melt inclusions lacking evidence of possible leakage and microlites larger than the vapour bubbles. However, in some cases we could not avoid inclusions with smaller microlites.

CO_2, H_2O, S, F and Cl concentrations in 29 melt inclusions and 16 matrix glass chips were measured by secondary ion mass spectrometry (SIMS) on a CAMECA IMS 1280 instrument at Woods Hole Oceanographic Institution. A high mass resolution (5000–6000 mass/Δmass) configuration ensured complete separation of the ^{12}C and $^{24}Mg^{2+}$ peaks. Sample preparation protocols and analytical procedures are outlined by Helo et al. (2011). Ten standard glasses, of basaltic and basaltic andesite compositions, were used to establish calibration curves for $^{12}C/^{30}Si$, $^{16}O^{1}H/^{30}Si$, $^{19}F/^{30}Si$, $^{32}S/^{30}Si$ and $^{35}Cl/^{30}Si$ versus the respective volatile component (Fig. S1, Table S1). The CO_2 content of all standard glasses was determined by Fourier transform infrared (FTIR) spectroscopy. The standard error on the slope of the calibration curves is 2.3% for CO_2 and 3.7% or better for H_2O, F, S and Cl. Repeated analyses (n=9) of our internal standard P1326-2, a Juan de Fuca Ridge basaltic glass, during our analytical session yielded 340 ± 24 (1σ) ppm CO_2, 0.29 ± 0.09 wt.% H_2O, 206 ± 6 ppm F, 1296 ± 26 ppm S, and 187 ± 5 ppm Cl (Fig. S2). This agrees well with values obtained by Helo et al. (2011). One outlier with 0.45 wt.% H_2O affects the standard deviation for water. Spot analyses of olivine adjacent to melt inclusions gave 40 ± 15 ppm CO_2, 0.06 ± 0.00 wt.% H_2O, 21 ± 2 ppm F, 1 ± 0 ppm S, and 2 ± 0 ppm Cl, demonstrating low analytical backgrounds. Further details on SIMS data quality and error propagation are provided in the Supplementary Materials.

After SIMS analysis, major element compositions of melt inclusions, glasses and olivine were acquired using a JEOL 8900 electron microprobe (EMPA) at McGill University and are given by Longpré et al. (2014). We used the same instrument and the method of Wallace and Carmichael (1994) to measure sulphur speciation in a subset of 17 melt inclusions and 13 matrix glass chips. Scans of the S*K*α wavelength were done from 171.517 to 172.478 mm λ with a step size of 3 µm and a dwell time of 0.55 s per step (total 176 s), using a 15 µm beam, a beam current of 20 nA, and an acceleration voltage of 15 kV. Peak shifts of unknowns were measured relative to a sphalerite (ZnS) standard. Anhydrite ($CaSO_4$) and barite ($BaSO_4$) standards were used to measure the maximum shift. In an attempt to quantify possible reduction or oxidation of sulphur upon exposure to the electron beam (Jugo et al., 2010; Klimm et al., 2012; Métrich and Clocchiatti, 1996; Rowe et al., 2007), we performed a series of tests using synthetic and natural glasses, the sulphur speciation of which had previously been measured by XANES and other methods (e.g., Fiege et al., 2015). These tests, fully presented in the Supplementary Materials (Figs. S3–S4, Table S2), suggest that (1) our EMPA-based method may significantly underestimate $S^{6+}/\Sigma S$ ratios for oxidised samples (here $S^{6+}/\Sigma S \geq 0.5$) (e.g., Jugo et al., 2010), (2) beam-induced oxidation of sulphur is negligible in our glasses (cf. Klimm et al.,

2012; Rowe et al., 2007), and (3) reproducibility of $S^{6+}/\Sigma S$ measurements for sulphur-rich glasses is within 10%, which we assign as a 1σ error for unknowns.

Trace element concentrations were obtained by laser ablation inductively coupled plasma mass spectrometry (LA-ICP-MS) at the University of Bremen (matrix glasses), with a New Wave UP193-SS laser coupled to a Thermo Finnigan Element2 mass spectrometer, and Lamont-Doherty Earth Observatory (15 melt inclusions and matrix glasses), with a New Wave UP193-FX laser coupled to a Thermo VG PQ ExCell mass spectrometer. Calibration curves were obtained using international basaltic glass standards, and repeated in-run analyses of secondary glass standards indicate that our data are accurate to better than 10% for most elements (see Supplementary Materials for further details).

Melt inclusion compositions were corrected, where applicable, for post-entrapment crystallisation of the host mineral on the inclusion walls and subsequent diffusive re-equilibration using the method of Danyushevsky et al. (2000) (see details in Supplementary Materials). On average, the correction procedure involved addition of 6% olivine. In the text and figures we present the corrected data, while both the raw and corrected data are listed in full in the Supplementary Materials. As discussed in sections 3.3 and 3.5, we also explored the effects of shrinkage bubble and sulphide bleb formation on the respective CO_2 and S budgets of the melt inclusions. These corrections, shown to be potentially important for CO_2 but relatively minor for S, are presented in the Supplementary Materials but were not applied to data reported in the text and figures.

3. Results and Discussion

3.1. Petrogenetic relationship between melt inclusions, matrix glasses and the bulk lava

Before discussion of volatile element systematics, it is useful to assess the petrogenetic relationship between the melt inclusions, the matrix glasses and the bulk lava. Olivine-hosted melt inclusions show a strong compositional affinity with bulk lava balloons, both in terms of major elements and elevated concentrations of incompatible trace elements (Fig. 3) (Longpré et al., 2014; Martí et al., 2013). In comparison, matrix glasses have lower MgO and even more enriched trace element concentrations. In the context of other mafic lavas from the Canaries, the 2011–2012 melt inclusions and bulk rocks appear typical for the western islands (El Hierro and La Palma), whereas lavas from the central islands (La Gomera, Tenerife and Gran Canaria) show lower incompatible trace element concentrations (Figs. 1, 3b) (Day et al., 2010; Gurenko et al., 2006). In comparison to glasses from Loihi and Kilauea volcanoes, Hawaii (Dixon and Clague, 2001; Sides et al., 2014), the El Hierro glasses are markedly more enriched.

The trace element data clearly indicate the olivine-hosted melt inclusions to be co-genetic to the 2011–2012 magma. In detail, the weak positive correlation of trace element enrichment proxies, such as the Ce/Y ratio, and trace element concentration (cf. Neave et al., 2014) suggests that the olivine-hosted melt inclusions represent variably enriched, but overall closely-related melts that mixed to produce the 2011–2012 bulk magma, which evolved via crystallisation of olivine, clinopyroxene and ulvöspinel to produce a residual melt — the matrix glass. Therefore, a melt more evolved than the matrix glasses likely did not participate in magma mixing below El Hierro in 2011–2012, and the origin of evolved (up to basaltic trachyandesite) ulvöspinel-hosted melt inclusions (cf. Longpré et al., 2014) will be re-evaluated elsewhere. We concur with Meletlidis et al. (2015) that data are consistent with a single batch of magma, with mixing of similar basanitic melts and entrainment of antecrysts producing zoned crystals and crystal cumulus in the magma body yielding an increase in crystal (and MgO) content with time in the bulk lava. The diffusion chronometry results of Longpré et al. (2014) record mobilisation of this magma batch shortly prior to and during eruption.

3.2. A volatile-rich magma

Olivine-hosted melt inclusions exhibit a wide range of volatile contents extending to high concentrations, revealing the volatile-rich nature of the 2011–2012 magma. Carbon dioxide concentrations in melt inclusions vary from 60 to 3420 ppm, with 50% of values above 1000 ppm CO_2. Dissolved water and sulphur contents are positively correlated and show ranges of 0.4–3.0 wt.% and 520–5080 ppm, respectively (Figs. 4–5). Concentrations of 1200–2210 ppm F and 580–1210 ppm Cl are positively correlated (Fig. 6). To our knowledge, these CO_2 and H_2O concentrations are the highest ever measured in melt inclusions from an ocean island volcano (e.g., Hauri, 2002; Métrich and Wallace, 2008), but are similar to those reported for other alkaline volcanoes such as Etna and Erebus (Oppenheimer et al., 2011; Spilliaert et al., 2006). Similarly high sulphur contents have been reported for submarine samples off the island of Gran Canaria (Gurenko and Schmincke, 2000), and so Canary Island magmas appear to be particularly sulphur-rich. In comparison to melt inclusions, matrix glasses contain much lower CO_2 (50–490 ppm), H_2O (0.4–1.0 wt.%) and S (420–1030 ppm) concentrations (Figs. 4–5), indicating extensive syn-eruptive degassing of these components. In contrast, the highest F and Cl concentrations in the El Hierro matrix glasses (1810–2140 ppm F and 920–1020 ppm Cl) are similar to those of olivine-hosted melt inclusions, implying little to no degassing of halogens (Fig. 6).

Estimates of undegassed volatile concentrations in basaltic magmas may be derived from lithophile trace element proxies, such as Nb (or Ba), Ce and Dy, which are thought to behave similarly to carbon, water and sulphur, respectively, during partial melting and crystallisation (Rosenthal et al., 2015; Saal et al., 2002). However, the CO_2/Nb and S/Dy systematics of basaltic melts should reflect the interplay between melting of C-bearing and S-bearing accessory minerals and melting of silicates

(Dasgupta and Hirschmann, 2010; Dasgupta et al., 2007) and so will in part be controlled by the original abundances of carbonates (or diamond) and sulphide in the source, which will vary in a heterogeneous mantle. We thus expect mantle volatile/lithophile trace element ratios to diverge geographically (e.g., Helo et al., 2011). In this context, the mantle CO_2/Nb and S/Dy ratios of 240 ± 50 and 225 ± 50, respectively, derived from the Siqueiros melt inclusions representing high-degree, ultra-depleted melts (Saal et al., 2002) are unlikely to pertain to the low-degree, enriched melts recorded by the El Hierro melt inclusions. A CO_2/Nb of 500 ± 170 (Rosenthal et al., 2015) and a S/Dy of 370 ± 90 (McDonough and Sun, 1995), thought to be representative of primitive mantle, may be more appropriate for enriched ocean island basalts. In comparison, measured CO_2/Nb ratios in the 2011–2012 olivine-hosted melt inclusions are much lower, ranging from 0.7 to 42 (Fig. 7a), which suggests that undegassed CO_2 concentrations in El Hierro basanite greatly exceeded observed values. A simple linear extrapolation to an undegassed CO_2/Nb ratio of 500 ± 170 yields primitive CO_2 contents in the range 2.5–5.0 wt%. This implies that ≥ 85% of the original CO_2 is missing from the melt inclusions and that carbon is a major constituent of primitive Canary Island magmas at depth, which is consistent with predictions of Dixon (1997). In contrast to the CO_2/Nb ratio, S/Dy ranges from 110 to 840, reaching or even exceeding estimated mantle values (McDonough and Sun, 1995), whereas the upper end of observed H_2O/Ce ratios (30 to 280) are similar to undegassed values for mid-ocean ridge and ocean island basalts (155–280) (e.g., Michael, 1995; Saal et al., 2002). This suggests that the highest H_2O (3.05 wt%) and S (5080 ppm) concentrations in El Hierro melt inclusions may be minimally degassed (Fig. 7b, c).

3.3. Deep CO_2 degassing and pressures of melt inclusion entrapment

The high volatile-carrying capacity of the El Hierro basanite is consistent with experimental data demonstrating the strong positive effect of alkalinity on CO_2 solubility (e.g., Dixon, 1997; Shishkina et al., 2014) (Fig. 4e). For the inferred primitive CO_2 concentrations reaching weight percent levels, exsolution of a CO_2-rich fluid begins at pressures in excess of 1 GPa, in agreement with fluid inclusion data reported by Hansteen et al. (1991). For the observed CO_2 concentrations, however, calculated vapour saturation pressures are relatively modest, with 3420 ppm CO_2 corresponding to 260–630 MPa depending on model (Iacono-Marziano et al., 2012; Newman and Lowenstern, 2002; Papale et al., 2006; Shishkina et al., 2014) and melt composition assumptions, particularly $Fe^{3+}/\sum Fe$ ratios (Fig. 4d). The model of Shishkina et al. (2014) is particularly well calibrated for basanitic compositions and yields an overall saturation pressure range of 8–280 MPa for olivine-hosted melt inclusions. However, for consistency with subsequent degassing modelling, we adopt the model of Iacono-Marziano et al. (2012), which is implemented into the D-Compress software (Burgisser et al., 2015). This gives a similar range of pressures of 7 to 260 MPa, i.e., within the upper 10 km beneath El Hierro. This is at odds with fluid inclusion and clinopyroxene–melt barometry indicating crystallisation,

and hence melt inclusion entrapment, in the uppermost mantle, consistent with pre- and syn-eruptive seismicity (Fig. 4c) (Longpré et al., 2014). Most notably, CO_2-rich fluid inclusions record pressures between 280 and 580 MPa, with most of values above 400 MPa corresponding to the local Moho at 13–15 km depth. This requires that the El Hierro basanite had already begun exsolving a CO_2-rich fluid at depths of at least 20 km.

Despite the significant uncertainties associated with any barometric method [e.g., fluid inclusion-derived pressures are dependent upon the chosen equation of state (Hansteen and Klügel, 2008) and clinopyroxene-melt barometry has a standard error of estimate of 150–200 MPa for calibration data and somewhat higher for global experimental datasets (Putirka, 2008)], we argue that the complete lack of overlap between pressures derived from CO_2 and H_2O contents in melt inclusions and other barometric methods considered here cannot solely be attributed to model errors. We envisage two possible explanations for this discrepancy:

(1) Calculated volatile saturation pressures could underestimate melt inclusion entrapment pressures because CO_2 originally dissolved in the melt might have later diffused into bubbles, which are ubiquitous in our samples (Fig. 2). Indeed, recent work has highlighted the possibility that inclusion-hosted bubbles, which are thought to form in response to post-entrapment processes affecting the inclusions (see summary by Hartley et al., 2014), may sometimes contain a large fraction of the CO_2 that was originally dissolved in the silicate melt upon entrapment (Hartley et al., 2014; Moore et al., 2015). Mean bubble to melt inclusion volume ratios in the El Hierro samples are 0.05 ± 0.02, at the upper end of values reported for olivine-hosted melt inclusions elsewhere (Hartley et al., 2014; Moore et al., 2015; Neave et al., 2015). A theoretical estimate of how much CO_2 may be sequestered in the bubble can be obtained using the method of Shaw et al. (2008) based on the ideal gas law. This calculation, presented in full in the Supplementary Materials, suggests that ~85% of the originally dissolved CO_2 (but minor H_2O) may be present in bubbles, yielding reconstructed CO_2 concentrations of up to 2.3 wt%. This would imply melt inclusion entrapment at high pressures (see Fig. 4d). As outlined by Neave et al. (2014) and Moore et al. (2015), however, this approach likely provides an upper bound for the amount of CO_2 sequestered in the bubble, because gas–melt equilibrium may not have been attained during rapid quenching of the melt inclusions. In addition, we note that the majority of bubbles investigated by Raman spectroscopy so far actually did not contain detectable CO_2 (cf. Hartley et al., 2014; Moore et al., 2015; Neave et al., 2014; Neave et al., 2015).

(2) Alternatively, melt inclusions entrapped at mantle depths corresponding to pressures indicated by clinopyroxene–melt and fluid inclusion geobarometry could have lost volatiles during ascent-driven decompression before sealing off at variable crustal pressures. This implies either incomplete closure of the melt inclusions at depth or decrepitation of the inclusions followed by healing

at different depths (Métrich and Wallace, 2008). Neave et al. (2015) came to the similar conclusion that melt inclusions from Grímsvötn, Iceland, must have lost CO_2 upon ascent to shallow depths. If this second possibility is correct, bubbles in El Hierro melt inclusions do not contain significant amounts of CO_2, but most of the originally dissolved CO_2 was lost by deep degassing of the primitive basanite prior to final melt inclusion entrapment. Distinguishing between possibilities (1) and (2) would require measurements of CO_2 in bubbles by Raman analysis, which is beyond the scope of this study. Scenario (2), however, is supported by evidence for concurrent H_2O and S degassing at pressures ≤300 MPa and is therefore favoured (see section 3.5, and Figs. 5b, 9a).

3.4. CO_2 supersaturation in matrix glasses

A closer look at matrix glasses reveals that the extensive carbon degassing discussed above was nevertheless incomplete. Figure 4b shows that all individual matrix glass analyses yielded CO_2 contents significantly in excess of 30 ppm, the expected maximum concentration for an eruption depth of 300 m below sea level (3 MPa) (Iacono-Marziano et al., 2012). Thus, the magma was supersaturated in CO_2 when it reached the surface and erupted. Disequilibrium degassing during rapid magma ascent will result in such CO_2 supersaturation (e.g., Paonita and Martelli, 2006). We note that matrix glasses from the earliest eruption products are characterised by the highest CO_2, which likely reflects higher magma ascent rate, consistent with shorter diffusion timescales obtained at the outermost rims of olivines from early samples (cf. Longpré et al., 2014).

3.5. Sulphur systematics

In contrast to most mid-ocean ridge and ocean island basalts (e.g., Wallace and Edmonds, 2011), sulphur concentrations at El Hierro are not correlated with melt iron content and far exceed the expected sulphur concentration at sulphide saturation (SCSS) of 1520–2650 ppm calculated with the model of Fortin et al. (2015) (which we select because it accounts for the effect of H_2O content on the SCSS) over a wide range of pressures (0.1–300 MPa), temperatures (1100–1200 °C), and water contents (0–3.5 wt%) (Fig. 5a, b). At first glance this seems at odds with the presence of sulphides in the samples (Fig. 2). However, the apparently high SCSS in the El Hierro magma is reconciled by the appreciable amounts of dissolved sulphate (Fig. 5c), which is much more soluble than sulphide in silicate melts (e.g., Wallace and Edmonds, 2011). Starting with a SCSS of 1520–2020 ppm when all sulphur is dissolved as S^{2-}, the model of Jugo (2009) (his equation 5) predicts an increased SCSS of 6720–8980 ppm for $S^{6+}/\Sigma S = 0.7$, consistent with our data. Substantial concentrations of dissolved sulphate appear common in Canary Island magmas (Bryan et al., 2002; Cooper et al., 2015; Gurenko and Schmincke, 2000; Parat et al., 2011). In a study of submarine glasses from Samoa, Labidi et al.

(2015) proposed that high $S^{6+}/\Sigma S$ ratios in arc and ocean island basalts may reflect the oxidising effect of melt water content on dissolved sulphur species.

Remarkably, both sulphur concentration and the $S^{6+}/\sum S$ ratio in El Hierro melt inclusions are positively correlated with water content (Fig. 5b, c, d). The preservation of these correlations rules out any significant influence of post-entrapment diffusion of H^+ (e.g., Bucholz et al., 2013) in controlling the H_2O content of melt inclusions. To a first order, mixing of volatile-rich and degassed melts, followed by melt entrapment at variable pressures, could potentially produce the linear relationships observed in Figure 5. However, simple degassing-induced crystallisation offers a simpler explanation to the broad negative correlations of H_2O and S with incompatible elements, such as Na (Fig. 5a inset), K, or Nb. Therefore, assuming that the melt inclusions are genetically related to each other and to the matrix glass and that the initial melt composition is best represented by the most volatile-rich inclusion, a process or processes must have caused a concurrent decrease in S and H_2O concentrations and the $S^{6+}/\sum S$ ratio in the melt. In Figure 8, we illustrate scenarios 1–4 considered by Marini et al. (2011) (see their Figure 14) that result in S loss in the melt with expected associated changes in $S^{6+}/\sum S$:

(1a) $SO_4^{2-}{}_{(melt)} \leftrightarrow SO_{2(gas)} + O^{2-}{}_{(melt)} + ½O_{2(gas)}$

(1b) $SO_4^{2-}{}_{(melt)} + Ca^{2+}{}_{(melt)} \leftrightarrow CaSO_{4(anhydrite)}$

(2) $3SO_4^{2-}{}_{(melt)} + S^{2-}{}_{(melt)} \leftrightarrow 4SO_{2(gas)} + 4O^{2-}{}_{(melt)}$

(3) $SO_4^{2-}{}_{(melt)} + S^{2-}{}_{(melt)} + H_2O_{(gas)} \leftrightarrow H_2S_{(gas)} + SO_{2(gas)} + 2O^{2-}{}_{(melt)} + ½O_{2(gas)}$

(4a) $S^{2-}{}_{(melt)} + H_2O_{(gas)} \leftrightarrow H_2S_{(gas)} + O^{2-}{}_{(melt)}$

(4b) $S^{2-}{}_{(melt)} + Fe^{2+}{}_{(melt)} \leftrightarrow FeS_{(liquid\ or\ pyrrhotite)}$

Of the above scenarios, only degassing of oxidised sulphur (1a) or anhydrite precipitation (1b) appear able to reproduce the S versus $S^{6+}/\Sigma S$ melt inclusion array. As melt S concentration decreases, reaction (2) produces a decrease in $S^{6+}/\Sigma S$ that is too small to account for the observed variations. Reactions (3), (4a) and (4b) result in increasing $S^{6+}/\Sigma S$ with decreasing S content, opposite to our observations. As regards reaction (4b), however, the common presence of single ≤ 5 μm sulphide spheres within the El Hierro melt inclusions (Fig. 2b) deserves further attention. High-resolution petrographic measurements show that the size of these sulphides is a constant fraction of the melt inclusion volume, i.e., 0.1 ± 0.1 vol%, suggesting a common formation mechanism post-dating melt inclusion entrapment. Danyushevsky et al. (2002) argued that such sulphide blebs may form in response to a decrease in sulphur solubility brought about by Fe loss from olivine-hosted melt inclusions, and we envisage a similar scenario for our suite of inclusions. We thus conclude that

reaction (4b) did occur in many of our melt inclusions, but had a minor effect on the observed sulphur systematics, as corroborated by mass balance calculations (see details in the Supplementary Materials, Fig. S6). In this context and since anhydrite is not observed in the El Hierro samples, ruling out reaction (1b), it is tempting to conclude that transfer of oxidised sulphur (S^{6+} dissolved as SO_4^{2-}) from the melt to SO_2 gas, in which sulphur occurs as S^{4+}, coupled to simultaneous H_2O degassing generated the trends observed in Figure 5. However, depictions of the effects of reactions 1–4 in Figure 8 treat the system as a finite pool of reduced and oxidised sulphur species, but sulphur speciation in silicate melts is sensitive to oxygen fugacity (fO_2) and, hence, a redox reaction could impose a new $S^{6+}/\Sigma S$ to the system.

3.6. Magma redox

Based on the model of Jugo et al. (2010), we computed fO_2 values using the $S^{6+}/\Sigma S$ ratio as a proxy. H_2O- and S-rich melt inclusions with a high $S^{6+}/\Sigma S$ ratio should record a higher fO_2 (up to ΔFMQ + 1.2, where ΔFMQ refers to the fO_2 of the sample relative to the fayalite–magnetite–quartz buffer in log units) than H_2O- and S-poor melt inclusions and matrix glasses with low $S^{6+}/\Sigma S$ (down to ΔFMQ + 0.2). In comparison, two-oxide thermobarometry and olivine–liquid equilibrium using crystal rims suggest more oxidising conditions of ΔFMQ + 1.8 and + 2.6, respectively, corresponding to $Fe^{3+}/\Sigma Fe$ ratios of 0.20 and 0.26 based on the expression of Kress and Carmichael (1991) (Longpré et al., 2014). We consider it likely that high-end fO_2 estimates obtained with these different methods may overlap within errors. Blundy and Cashman (2008) computed an average absolute deviation of ~0.3 log units for the two-oxide thermobarometer of Ghiorso and Evans (2008), but errors associated with the other two methods are difficult to quantify. Because of potential photo-reduction of S during electron microprobe analysis (with the possible counter-effect of post-entrapment sulphide formation), our $S^{6+}/\Sigma S$ data may underestimate maximum fO_2 (see section 2 and Supplementary Materials). However, as sulphur speciation in silicate melts can change extremely rapidly (Métrich et al., 2009), $S^{6+}/\Sigma S$ measurements may track late-stage fO_2 variability not recorded by mineral–mineral or mineral–melt thermobarometers. In this context, the melt inclusions appear to capture a reduction of the magma oxidation state by at least one log unit of fO_2 upon ascent and degassing. Moussallam et al. (2014) reported a similar situation for basanitic to phonolitic samples from Erebus volcano, Antarctica. These authors observed a positive correlation of $Fe^{3+}/\Sigma Fe$ ratios (measured by XANES) in melt inclusions and calculated vapour saturation pressures, translating into a decrease of fO_2 by more than 2 log units during magma ascent and degassing.

To quantify the degassing process and its impact on fO_2 evolution, we conducted a series of simulations using the D-Compress software (Burgisser et al., 2015). The El Hierro matrix glass was used as melt composition with initial CO_2 and H_2O concentrations of 3420 ppm and 3.05 wt%,

respectively, at 300 MPa, 1150 ˚C, and fO_2 = FMQ + 1.2 and +1.7. Notably, initial melt sulphur concentration is not an input in D-Compress; it is computed based on implemented solubility laws. The key results of these degassing models, distilled in Figure 9, are as follows. (1) Coupled S and H_2O degassing reproduces the S vs. H_2O melt inclusion array and is predicted to begin at relatively high pressure (300 MPa) (cf. Lesne et al., 2011). (2) All realistic open system and closed system degassing scenarios yield a net decrease in melt fO_2 upon decompression, consistent with our $S^{6+}/\sum S$ data (Fig. 5c). This strongly supports our conclusion that extensive decompression-driven S and H_2O degassing of the El Hierro basanite caused a significant reduction of its oxidation state.

It remains difficult to pinpoint the specific reactions governing this redox change. Moussallam et al. (2014) concluded that sulphur degassing is driving the redox evolution of Erebus magmas according to the following reactions:

(5) $S^{2-}_{(melt)} + 3Fe_2O_{3\,(melt)} \leftrightarrow SO_{2(gas)} + 6FeO_{(melt)} + O^{2-}_{(melt)}$

(6) $SO_4^{2-}{}_{(melt)} + 2FeO_{(melt)} \leftrightarrow SO_{2(gas)} + Fe_2O_{3\,(melt)} + O^{2-}_{(melt)}$

Based on the observed decrease in $Fe^{3+}/\sum Fe$ ratios at Erebus, these authors favoured reaction (5). As this reaction proceeds to the right, the melt is reduced via SO_2 degassing and, consequently, melt $S^{6+}/\sum S$ will re-equilibrate to a new, lower fO_2. This is consistent with XANES spectra for sulphur indicating that Erebus melts entrapped at higher pressures are characterised by both higher $Fe^{3+}/\Sigma Fe$ and $S^{6+}/\Sigma S$ (Moussallam et al., 2014). Preliminary XANES data for El Hierro samples also show that melt inclusions have higher $Fe^{3+}/\Sigma Fe$ ratios than degassed matrix glasses (Y. Moussallam, personal communication 2015), mirroring our $S^{6+}/\sum S$ data and consistent with an important role for reaction (5).

3.7. Sulphide saturation

The occurrence of large, conspicuous sulphide globules as inclusions near the rims of clinopyroxene and ulvöspinel (Fig. 2c) appears to record sulphide saturation in the El Hierro magma. In contrast, the tiny inclusion-hosted sulphides discussed above most likely formed in response to post-entrapment modification of melt inclusion composition and thus have little to do with bulk melt sulphide saturation. The virtual absence of the large sulphide inclusions in olivine (inspection of several hundred olivine grains in the course of this study returned a single sulphide inclusion) and as free floating blebs in matrix glass may suggest that sulphide saturation occurred late, but that sulphides ultimately became unstable and were (re)dissolved in the silicate melt or scavenged by a gas phase prior to eruption. The cause and timing of sulphide saturation in the sulphur-rich El Hierro basanite are thus intriguing, and we here outline three possibilities. (1) Sulphide saturation was caused by magnetite crystallisation. Jenner et al. (2010) presented a compelling case for the

potentially important role of magnetite crystallisation and associated reduction of the melt in triggering sulphide saturation in arc-related magmas. If this process was dominant at El Hierro, we would expect a positive correlation between iron content and the $S^{6+}/\sum S$ ratio in melt inclusions. But these variables are weakly negatively correlated (Fig. S7), with a drop in FeO observed for matrix glasses only, suggesting that ulvöspinel crystallisation did not affect the composition of most olivine-hosted melt inclusions and did not drive the decrease in $S^{6+}/\sum S$ ratio. A subtle change in slope in the S versus FeO trend at ~1500 ppm S could reflect the late onset of coincidental ulvöspinel crystallisation and sulphide formation (Fig. 5a). (2) Sulphide saturation was caused by a diffusion-controlled enrichment of sulphur at the crystal–melt interface (Bacon, 1989). In this case, sulphide saturation would have been reached only locally, in the vicinity of growing crystals, resulting in the formation and subsequent trapping of sulphide globules. While this possibility is consistent with the lack of sulphides in the matrix glass, it calls for an unknown mechanism — although potentially related to differential crystal growth rates — to produce abundant sulphides in ulvöspinel and clinopyroxene and essentially none in olivine. (3) The degassing-induced decrease in fO_2 and associated drop in SCSS (e.g., Jugo, 2009) caused sulphide saturation. As illustrated in Figure 5c, the SCSS is drastically reduced upon decrease of the $S^{6+}/\sum S$ ratio in the melt. In our preferred scenario, the initially oxidised, sulphide-undersaturated El Hierro magma became sulphide-saturated during degassing as the decrease in SCSS outpaced sulphur loss.

3.8. Implications for the mantle source and origin of volatiles

Several lines of evidence, including high TiO_2 contents (Prytulak and Elliott, 2007), multiple isotopic proxies (Day et al., 2010; Day et al., 2009; Sigmarsson et al., 1998) and olivine compositions (Gurenko et al., 2009), suggest that the mantle source of El Hierro and other Canary Island lavas contains significant amounts of recycled oceanic crust, in the form of pyroxenite or eclogite. Day et al. (2009) estimated the amount of recycled oceanic lithosphere present in the source of El Hierro at <10%, and Day et al. (2010) presented a partial melting model, using La/Yb and Dy/Yb systematics, which indicates that 2–6 % melting of an enriched source, beginning in the garnet stability field at ≥110 km depth and extending into the spinel stability field, can account for the trace element characteristics of Pleistocene and Holocene El Hierro and La Palma lavas. La/Yb and Dy/Yb ratios for the 2011–2012 samples are 26.0 ± 3.0 and 3.4 ± 0.4, respectively, overlapping with data reported by Day et al. (2010), therefore suggesting similar melting conditions. We note, however, that melting of carbonated peridotite at high pressure may also play a role in the genesis of El Hierro lavas (Dasgupta et al., 2007).

The high pressure — both calculated and inferred — of initial saturation with a CO_2-rich fluid and the enrichment of volatile and non-volatile incompatible elements in the El Hierro basanite indicate that the bulk of volatiles originate from the mantle. Simple batch melting models illustrate the feasibility

of generating high initial volatile concentrations by low degrees of partial melting; mismatch by one order of magnitude of predicted versus observed CO_2 concentrations reinforces our conclusion that appreciable amounts of CO_2 are missing from melt inclusions (Fig. 10). In addition, low Cl/K ratios (0.07 ± 0.01) for El Hierro melt inclusions and matrix glasses rule out a significant volatile contribution from shallow, seawater-influenced components, such as brines, as suggested for some MORB and Hawaiian glasses (e.g., Kent et al., 1999). Finally, for both El Hierro (this work) and Gran Canaria (Gurenko and Schmincke, 2000), the most primitive, volatile-rich melt inclusions also show the highest $S^{6+}/\sum S$ ratios, which leads us to propose that the Canary mantle source may be particularly oxidised, such as inferred for Erebus volcano (Moussallam et al., 2014). This is in agreement with major element systematics indicating that Canary Island magmas are generally more oxidised than archetypal ocean island basalts from Hawaii and Iceland (Herzberg and Asimow, 2008).

3.9. Eruption style, volatile yields and environmental impact

We propose that initially high volatile contents and intense shallow level degassing led to submarine Strombolian-type explosive activity at El Hierro. This is consistent with the construction of a 200–300-m-tall submarine cone (Rivera et al., 2013) and strong bubbling at the ocean surface, and it lends support to an (mildly) explosive origin of lava balloons (Kelly et al., 2014). Based on an eruptive volume of 329 × 10^6 m^3 (Rivera et al., 2013) converted to ~160–260 × 10^6 m^3 of dense magma assuming a deposit porosity of 20–50%, a magma crystallinity of 15%, a magma density of 2,900 kg/m^3 and assuming 3200 ppm CO_2 and 4500 ppm S total degassing, we estimate that the El Hierro eruption released at least 1.3–2.1 Tg CO_2 and 1.8–2.9 Tg S to the environment. We emphasise that these figures must be regarded as minima, particularly for CO_2. However, the late formation of sulphide globules may have provided a sink for some of the sulphur. For comparison, Santana-Casiano et al. (2013) calculated a CO_2 output of 0.05 Tg/day for the week of 4–9 November 2011 based on pCO_2 values measured in the seawater column in the vicinity of the vent. Extrapolating such CO_2 discharge over the entire course of the eruption (147 days) yields 7.4 Tg CO_2. This is likely an upper limit for the CO_2 yield, as the week of 4–9 November coincided with the most intense bubbling and degassing at the sea surface. Degassing of the El Hierro basanite caused dramatic decreases in seawater pH in the vicinity of the vent from a background of 8.0 to a low of 5.1, and anomalously high concentrations of dissolved reduced sulphur species were also detected in the water column (Santana-Casiano et al., 2013). On land, detected diffuse CO_2 emissions were comparatively small, with an estimated 1.1 × 10^{-4} Tg CO_2 for the July 2011–March 2012 period (Melián et al., 2014).

Our calculated CO_2 yield corresponds to at least 1–7% of the estimated annual flux of 29–154 Tg CO_2 from mid-ocean ridges and ocean islands (Kelemen and Manning, 2015). And while deep sulphur fluxes from mid-ocean ridges and ocean islands are poorly constrained at present, the S yield

of the 2011–2012 eruption equates to 17–28% of Andres and Kasgnoc (1998)'s estimate for the time-averaged global subaerial emissions of 10.4 Tg/yr S and 23–38% of Shinohara's (2013) 7.7 Tg/yr S value for subduction zones only. Therefore, despite its modest volume, representing about 1–2% of the annual magma output at mid-ocean ridge and ocean island volcanoes (Crisp, 1984), the 2011–2012 El Hierro eruption transferred significant amounts of volatiles to the Earth's surface.

4. Conclusions

In summary, we document some of the highest volatile concentrations ever measured in silicate melt inclusions from an ocean island volcano. Prior to deep degassing, CO_2 concentrations in the parental 2011–2012 El Hierro magma likely reached weight percent levels; we envisage carbon to be a major constituent of primitive Canary Island magmas. The most primitive, least-degassed melt inclusions are oxidised, and we suggest that this is inherited from the mantle source. Coupled H_2O and S degassing beginning at pressures of at least 300 MPa, and continuing up to the surface, caused a strong late-stage reduction of the oxidation state of the basanite by about 1 log unit of fO_2. In turn, this change in magma redox reduced sulphur solubility to the point of sulphide saturation, producing abundant sulphide globules. The large amounts of volatiles released by degassing of the 2011–2012 magma caused significant stress to the local ecosystem, reflected in seawater chemistry during the eruption. We propose that mafic alkaline volcanism in intraplate ocean island settings contribute large amounts of volatiles to the Earth surface.

Acknowledgements

We thank Instituto Geográfico Nacional personnel for support during fieldwork and for sharing lava balloon samples. The Cabildo de El Hierro – Medio Ambiente provided sampling permits. Brian Monteleone, Lang Shi, and Louise Bolge provided invaluable help during SIMS, electron microprobe and LA-ICP-MS analysis, respectively. Adrian Fiege generously provided experimental glasses for sulphur speciation tests. Discussions with Patrick Beaudry, Don Baker, Alain Burgisser, Jason Coumans, Thor Hansteen, Marion Le Voyer, Yves Moussallam and Terry Plank helped shape this paper. We also thank David Neave and Michael Rowe for thoughtful reviews and Tamsin Mather for editorial handling. This research was funded through a CUNY Research Foundation grant to M-AL, NSERC Discovery and Accelerator grants to JS, and a German Research Foundation (DFG) grant (KL1313/16) to AK.

Figure captions

Figure 1: The Canary Islands. The red triangle indicates the site of the 2011–2012 submarine eruption just south of El Hierro. The inset shows the location of the archipelago in the eastern Atlantic Ocean. Map constructed with GeoMapApp (www.geomapapp.org).

Figure 2: Photomicrographs of the El Hierro samples. a, Melt inclusion-bearing olivine crystal floating in matrix glass. **b**, Zoom on an olivine-hosted melt inclusion containing a bubble and a sulphide sphere. **c**, Sulphide inclusion occurring near rim of an ulvöspinel crystal.

Figure 3: Incompatible trace element enrichment. a, Ce/Y ratio versus Nb concentration for individual 2011–2012 olivine-hosted melt inclusions (this work), and average matrix glass (this work) and bulk rocks (BR) (Martí et al., 2013). Average bulk rock values for mafic lavas (40–50 wt% SiO_2) for El Hierro (EH), La Palma (LP), La Gomera (LG), Tenerife (TF) and Gran Canaria (GC) (Day et al., 2010; Gurenko et al., 2006) are also shown, as well as melt inclusion and matrix glass data for Hawaii (Dixon and Clague, 2001; Sides et al., 2014) and ocean floor basalt (OFB) glasses worldwide (Jenner and O'Neill, 2012). All error bars are ±1σ. **b**, Primitive mantle (PM)-normalised (McDonough and Sun, 1995) multi-element diagram with data groupings and sources as in (a), except that here the average is plotted for the El Hierro melt inclusions, Hawaii (split for Loihi and Kilauea volcanoes) and ocean floor basalts.

Figure 4: High-pressure CO_2 degassing. a, Dissolved CO_2 and H_2O concentrations in olivine-hosted melt inclusions (MI-ol) and average matrix glass measured by ion microprobe. Fully propagated error bars are shown (see Supplementary Information), except when smaller than symbol size. Isobars for 100, 200, 300 and 400 MPa are shown and were calculated with D-Compress (Burgisser et al., 2015) using the matrix glass composition and a temperature of 1150 °C. Data for Hawaii from Dixon and Clague (2001), Hauri (2002) and Sides et al. (2014). **b**, Zoom below 1000 ppm CO_2 on individual matrix glass analyses. October 15 matrix glasses contain more CO_2 than later samples but all are CO_2-supersaturated with respect to their eruption pressure of 3 MPa. Isobars for 3, 25, 50 and 100 MPa are shown. **c**, Histogram of depths (converted from pressures, see Longpré et al. (2014)) recorded by matrix glasses, melt inclusions, fluid inclusions (FI), clinopyroxene–melt geobarometry (Cpx) and pre- and syn-eruptive volcano-tectonic seismicity (EQ) (Longpré et al., 2014; IGN earthquake catalogue, www.ign.es). Vapour saturation pressures for matrix glasses and melt inclusions were calculated after Iacono-Marziano et al. (2012). **d**, Comparison of CO_2 solubility models. CO_2 solubility as a function of pressure was calculated at 1150 °C for the 2011–2012 average matrix glass composition, assuming equilibrium with a pure CO_2 fluid. SiO_2-corrected (45.06 wt%) VolatileCalc (Newman and Lowenstern, 2002) curve (1) is independent of melt iron content. However,

the model of Papale et al. (2006) requires FeO and Fe_2O_3 inputs, which exert strong control on CO_2 solubility. Curves (2) and (3) respectively assuming molar $Fe^{3+}/\Sigma Fe = 0$ (all iron as FeO) and $Fe^{3+}/\Sigma Fe = 0.26$ (plausible value based on olivine-glass equilibrium (Longpré et al., 2014)) are shown. The formulation of Shishkina et al. (2014) is weakly dependent on melt iron content and is used here assuming all iron as FeO (curve 4). Curve (5) shows the model of Iacono-Marziano et al. (2012). Note that the solubility models are generally not well calibrated above 500 MPa and so extrapolation to higher pressure is for illustration purposes only. **e**, Effect of composition on CO_2 solubility; CO_2 solubility (after Iacono-Marziano et al., 2012) as a function of pressure for El Hierro, average Kilauea and ocean floor basalt glass compositions.

Figure 5: Sulphur systematics. Sulphur concentration versus total iron (FeO*) (**a**), H_2O (**b**) and sulphur speciation (mole fraction of sulphate over total sulphur measured by electron microprobe) (**c**) in melt inclusions and matrix glasses. The inset in (a) shows S (same axis scale) versus Na_2O and the effect of concurrent degassing and crystallisation. Dotted lines in (b) show the sulphur concentration at sulphide saturation (SCSS) at $S^{6+}/\Sigma S = 0$ calculated after Fortin et al. (2015) at temperatures of 1100 (orange), 1150 (red) and 1200 °C (dark red) over a range of pressures (0.1–300 MPa) and H_2O contents (0–3.5 wt%) consistent with our data. The SCSS values at H_2O = 0 wt% (1520–2020 ppm S) were then extrapolated to higher $S^{6+}/\Sigma S$ in (c) using Equation 5 of Jugo (2009). **d**, H_2O content versus sulphur speciation. Data for ocean floor basalts and Hawaii as in Figures 3 and 4.

Figure 6: Behaviour of halogens. Fluorine and chlorine concentrations are positively correlated in El Hierro melt inclusions. The high concentration in matrix glass indicates that very little to no degassing of these elements occurred upon eruption. Data for Hawaii as in Figure 4.

Figure 7: Volatile/lithophile element systematics. Ratios of volatile and lithophile trace elements of similar compatibility are plotted against denominator concentrations and are compared to expected ratios for undegassed mantle melts (red dotted lines: McDonough and Sun, 1995; orange solid lines: Rosenthal et al., 2015; dark red dashed lines: Saal et al., 2002). **a**, CO_2/Nb versus Nb; **b**, H_2O/Ce versus Ce; and **c**, S/Dy versus Dy. Whereas H_2O/Ce and S/Dy ratios in El Hierro melt inclusions reach or exceed expected mantle values, CO_2/Nb ratios are much lower, suggesting extensive loss of CO_2. In all cases, broad negative correlations between volatile/lithophile ratios and incompatible trace element concentrations indicate the combined effect of degassing and crystallisation (labelled arrows in b), whereas displacement of the El Hierro data to the right of the diagrams, with respect to ocean floor basalts and Hawaii (data as in Figure 3), is due to lower degrees of melting of an enriched source.

Figure 8: Sulphur redox scenarios. Sulphur concentration versus speciation, melt inclusion data are shown by open circles. Curves labelled with numbers correspond to the effects of reactions (1), (2), (3) and (4), respectively, using initial conditions of 5080 ppm S and $S^{6+}/\sum S = 0.71$.

Figure 9: Degassing simulations. a and **b** sulphur concentration vs. H_2O content and fO_2 expressed as ΔFMQ, respectively. Degassing models calculated with D-Compress (Burgisser et al., 2015) are shown for open (dashed lines) and closed (solid lines) C–S–O–H–Fe systems using the matrix glass composition and initial conditions of 300 MPa, 1150 ˚C, 3420 ppm CO_2, 3.05 wt% H_2O, and fO_2 = FMQ + 1.2 (grey lines) or FMQ + 1.7 (black lines). **c** and **d** pressure vs. fO_2 during closed and open system degassing, respectively, with the effect of the system considered, either O–H, S–O–H, C–S–O–H or C–S–O–H–Fe, shown by curves of different colours. Calculations performed as for **a** and **b**, but only results for an initial fO_2 of FMQ + 1.2 are shown. For a closed system, only degassing in the O–H system yields to oxidation of the melt; in all other situations, reduction occurs. For an open system, degassing in the C–S–O–H–Fe system first produces a slight oxidation, then reduction at pressure below ~ 200 MPa; in all other cases, reduction occurs. In all panels, open circles show melt inclusion data, with fO_2 values calculated from $S^{6+}/\sum S$ ratios after Jugo et al. (2010) and saturation pressures after Iacono-Marziano et al. (2012).

Figure 10: Batch melting constraints on elemental concentrations in the El Hierro basanite. Simple batch melting calculations were performed assuming bulk peridotite/melt partition coefficients ($D^{peridotite/melt}$) of 0.00055 for CO_2, 0.011 for F, 0.00012 for Ba, 0.079 for Dy and 0.0034 for Nb (Rosenthal et al., 2015; Workman and Hart, 2005). $D^{peridotite/melt}$ for S is poorly constrained, but is thought to be similar to that of rare earth elements (Saal et al., 2002); curves with triangular and circular symbols assume behaviours similar to those of La ($D^{peridotite/melt}$ = 0.01) and Dy ($D^{peridotite/melt}$ = 0.079), respectively (Workman and Hart, 2005). Solid curves assume a source similar to primitive mantle (PM) with 600 ppm CO_2, 300 ppm S, 25 ppm F, 6.6 ppm Ba, 0.674 ppm Dy and 0.75 ppm Nb (McDonough and Sun, 1995; Rosenthal et al., 2015). Dashed lines are drawn for a depleted MORB mantle (DMM) source containing 75 ppm CO_2, 146 ppm S, 16 ppm F, 0.563 ppm Ba, 0.505 ppm Dy and 0.1485 ppm Nb (Rosenthal et al., 2015; Saal et al., 2002; Workman and Hart, 2005). Digits on curves refer to melt weight fractions in %. Data for the El Hierro basanite show the highest melt inclusion values for volatile elements (3420 ppm CO_2, 5080 ppm S, 2210 ppm F) and average bulk rock values from Martí et al. (2013) for non-volatile elements (390 ppm Ba, 7.4 ppm Dy, 68 ppm Nb).

References

Andres, R.J., Kasgnoc, A.D., 1998. A time-averaged inventory of subaerial volcanic sulfur emissions. Journal of Geophysical Research: Atmospheres 103, 25251-25261. doi:10.1029/98JD02091.

Bacon, C.R., 1989. Crystallization of accessory phases in magmas by local saturation adjacent to phenocrysts. Geochimica et Cosmochimica Acta 53, 1055-1066. doi:10.1016/0016-7037(89)90210-X.

Blundy, J., Cashman, K., 2008. Petrologic reconstruction of magmatic system variables and processes. Reviews in Mineralogy and Geochemistry 69, 179-239. doi:10.2138/rmg.2008.69.6.

Bryan, S.E., Martí, J., Leosson, M., 2002. Petrology and geochemistry of the Bandas del Sur Formation, Las Canadas edifice, Tenerife (Canary Islands). Journal of Petrology 43, 1815-1856. doi:10.1093/petrology/43.10.1815.

Bucholz, C.E., Gaetani, G.A., Behn, M.D., Shimizu, N., 2013. Post-entrapment modification of volatiles and oxygen fugacity in olivine-hosted melt inclusions. Earth and Planetary Science Letters 374, 145-155. doi:10.1016/j.epsl.2013.05.033.

Burgisser, A., Alletti, M., Scaillet, B., 2015. Simulating the behavior of volatiles belonging to the C–O–H–S system in silicate melts under magmatic conditions with the software D-Compress. Computers & Geosciences 79, 1-14. doi:10.1016/j.cageo.2015.03.002.

Carracedo, J.C., Troll, V.R., Zaczek, K., Rodríguez-González, A., Soler, V., Deegan, F.M., 2015. The 2011–2012 submarine eruption off El Hierro, Canary Islands: New lessons in oceanic island growth and volcanic crisis management. Earth-Science Reviews 150, 168-200. doi:10.1016/j.earscirev.2015.06.007.

Cooper, L.B., Bachmann, O., Huber, C., 2015. Volatile budget of Tenerife phonolites inferred from textural zonation of S-rich haüyne. Geology 43, 423-426. doi:10.1130/g36505.1.

Crisp, J.A., 1984. Rates of magma emplacement and volcanic output. Journal of Volcanology and Geothermal Research 20, 177-211. doi:10.1016/0377-0273(84)90039-8.

Danyushevsky, L.V., Della-Pasqua, F.N., Sokolov, S., 2000. Re-equilibration of melt inclusions trapped by magnesian olivine phenocrysts from subduction-related magmas: petrological implications. Contributions to Mineralogy and Petrology 138, 68-83. doi:10.1007/pl00007664.

Danyushevsky, L.V., McNeill, A.W., Sobolev, A.V., 2002. Experimental and petrological studies of melt inclusions in phenocrysts from mantle-derived magmas: an overview of techniques, advantages and complications. Chemical Geology 183, 5-24. doi:10.1016/s0009-2541(01)00369-2.

Dasgupta, R., Hirschmann, M.M., 2010. The deep carbon cycle and melting in Earth's interior. Earth and Planetary Science Letters 298, 1-13. doi:10.1016/j.epsl.2010.06.039.

Dasgupta, R., Hirschmann, M.M., Smith, N.D., 2007. Partial melting experiments of peridotite + CO_2 at 3 GPa and genesis of alkalic ocean island basalts. Journal of Petrology 48, 2093-2124. doi:10.1093/petrology/egm053.

Day, J., Pearson, D.G., Macpherson, C.G., Lowry, D., Carracedo, J.C., 2010. Evidence for distinct proportions of subducted oceanic crust and lithosphere in HIMU-type mantle beneath El Hierro and La Palma, Canary Islands. Geochimica et Cosmochimica Acta 74, 6565-6589. doi:10.1016/j.gca.2010.08.021.

Day, J.M., Pearson, D.G., Macpherson, C.G., Lowry, D., Carracedo, J.-C., 2009. Pyroxenite-rich mantle formed by recycled oceanic lithosphere: Oxygen-osmium isotope evidence from Canary Island lavas. Geology 37, 555-558. doi:10.1130/G25613A.1.

Dixon, J.E., 1997. Degassing of alkalic basalts. American Mineralogist 82, 368-378. doi:10.2138/am-1997-3-415.

Dixon, J.E., Clague, D.A., 2001. Volatiles in basaltic glasses from Loihi seamount, Hawaii: evidence for a relatively dry plume component. Journal of Petrology 42, 627-654. doi:10.1093/petrology/42.3.627.

Fiege, A., Holtz, F., Behrens, H., Mandeville, C.W., Shimizu, N., Crede, L.S., Göttlicher, J., 2015. Experimental investigation of the S and S-isotope distribution between H_2O–S±Cl fluids and basaltic melts during decompression. Chemical Geology 393, 36-54. doi:10.1016/j.chemgeo.2014.11.012.

Fortin, M.-A., Riddle, J., Desjardins-Langlais, Y., Baker, D.R., 2015. The effect of water on the sulfur concentration at sulfide saturation (SCSS) in natural melts. Geochimica et Cosmochimica Acta 160, 100-116. doi:10.1016/j.gca.2015.03.022.

640 Ghiorso, M.S., Evans, B.W., 2008. Thermodynamics of rhombohedral oxide solid solutions and a revision of the
641 Fe-Ti two-oxide geothermometer and oxygen-barometer. American Journal of Science 308, 957-1039.
642 doi:10.2475/09.2008.01.

643 Gurenko, A.A., Hoernle, K.A., Hauff, F., Schmincke, H.U., Han, D., Miura, Y.N., Kaneoka, I., 2006. Major, trace
644 element and Nd–Sr–Pb–O–He–Ar isotope signatures of shield stage lavas from the central and western Canary
645 Islands: Insights into mantle and crustal processes. Chemical Geology 233, 75-112.
646 doi:10.1016/j.chemgeo.2006.02.016.

647 Gurenko, A.A., Schmincke, H.-U., 2000. S concentrations and its speciation in Miocene basaltic magmas north
648 and south of Gran Canaria (Canary Islands): constraints from glass inclusions in olivine and clinopyroxene.
649 Geochimica et Cosmochimica Acta 64, 2321-2337. doi:10.1016/S0016-7037(00)00353-7.

650 Gurenko, A.A., Sobolev, A.V., Hoernle, K.A., Hauff, F., Schmincke, H.-U., 2009. Enriched, HIMU-type peridotite
651 and depleted recycled pyroxenite in the Canary plume: A mixed-up mantle. Earth and Planetary Science Letters
652 277, 514-524. doi:10.1016/j.epsl.2008.11.013.

653 Hansteen, T.H., Andersen, T., Neumann, E.-R., Jelsma, H., 1991. Fluid and silicate glass inclusions in ultramafic
654 and mafic xenoliths from Hierro, Canary Islands: implications for mantle metasomatism. Contributions to
655 Mineralogy and Petrology 107, 242-254. doi:10.1007/bf00310710.

656 Hansteen, T.H., Klügel, A., 2008. Fluid inclusion thermobarometry as a tracer for magmatic processes. Reviews
657 in Mineralogy and Geochemistry 69, 143-177.

658 Hansteen, T.H., Klügel, A., Schmincke, H.-U., 1998. Multi-stage magma ascent beneath the Canary Islands:
659 evidence from fluid inclusions. Contributions to Mineralogy and Petrology 132, 48-64.
660 doi:10.1007/s004100050404.

661 Hartley, M.E., Maclennan, J., Edmonds, M., Thordarson, T., 2014. Reconstructing the deep CO_2 degassing
662 behaviour of large basaltic fissure eruptions. Earth and Planetary Science Letters 393, 120-131.
663 doi:10.1016/j.epsl.2014.02.031.

664 Hauri, E., 2002. SIMS analysis of volatiles in silicate glasses, 2: isotopes and abundances in Hawaiian melt
665 inclusions. Chemical Geology 183, 115-141. doi:10.1016/s0009-2541(01)00374-6.

666 Helo, C., Longpré, M.-A., Shimizu, N., Clague, D.A., Stix, J., 2011. Explosive eruptions at mid-ocean ridges
667 driven by CO_2-rich magmas. Nature Geoscience 4, 260-263. doi:10.1038/ngeo1104.

668 Herzberg, C., Asimow, P.D., 2008. Petrology of some oceanic island basalts: PRIMELT2.XLS software for
669 primary magma calculation. Geochemistry, Geophysics, Geosystems 9, Q09001. doi:10.1029/2008GC002057.

670 Hudgins, T.R., Mukasa, S.B., Simon, A.C., Moore, G., Barifaijo, E., 2015. Melt inclusion evidence for CO_2-rich
671 melts beneath the western branch of the East African Rift: implications for long-term storage of volatiles in the
672 deep lithospheric mantle. Contributions to Mineralogy and Petrology 169, 1-18. doi:10.1007/s00410-015-1140-9.

673 Iacono-Marziano, G., Morizet, Y., Le Trong, E., Gaillard, F., 2012. New experimental data and semi-empirical
674 parameterization of H_2O–CO_2 solubility in mafic melts. Geochimica et Cosmochimica Acta 97, 1-23.
675 doi:10.1016/j.gca.2012.08.035.

676 Jenner, F.E., O'Neill, H.S.C., 2012. Analysis of 60 elements in 616 ocean floor basaltic glasses. Geochemistry,
677 Geophysics, Geosystems 13, Q02005. doi:10.1029/2011GC004009.

678 Jenner, F.E., O'Neill, H.S.C., Arculus, R.J., Mavrogenes, J.A., 2010. The magnetite crisis in the evolution of arc-
679 related magmas and the initial concentration of Au, Ag and Cu. Journal of Petrology 51, 2445-2464.
680 doi:10.1093/petrology/egq063.

681 Jugo, P.J., 2009. Sulfur content at sulfide saturation in oxidized magmas. Geology 37, 415-418.
682 doi:10.1130/g25527a.1.

683 Jugo, P.J., Wilke, M., Botcharnikov, R.E., 2010. Sulfur K-edge XANES analysis of natural and synthetic basaltic
684 glasses: Implications for S speciation and S content as function of oxygen fugacity. Geochimica et
685 Cosmochimica Acta 74, 5926-5938. doi:10.1016/j.gca.2010.07.022.

686 Kelemen, P.B., Manning, C.E., 2015. Reevaluating carbon fluxes in subduction zones, what goes down, mostly
687 comes up. Proceedings of the National Academy of Sciences 112, E3997-E4006.
688 doi:10.1073/pnas.1507889112.

Kelly, J.T., Carey, S., Pistolesi, M., Rosi, M., Croff-Bell, K.L., Roman, C., Marani, M., 2014. Exploration of the 1891 Foerstner submarine vent site (Pantelleria, Italy): insights into the formation of basaltic balloons. Bulletin of Volcanology 76, 1-18. doi:10.1007/s00445-014-0844-4.

Kent, A.J., Clague, D.A., Honda, M., Stolper, E.M., Hutcheon, I.D., Norman, M.D., 1999. Widespread assimilation of a seawater-derived component at Loihi Seamount, Hawaii. Geochimica et Cosmochimica Acta 63, 2749-2761. doi:10.1016/S0016-7037(99)00215-X.

Klimm, K., Kohn, S.C., O'Dell, L.A., Botcharnikov, R.E., Smith, M.E., 2012. The dissolution mechanism of sulphur in hydrous silicate melts. I: Assessment of analytical techniques in determining the sulphur speciation in iron-free to iron-poor glasses. Chemical Geology 322–323, 237-249. doi:10.1016/j.chemgeo.2012.04.027.

Kress, V.C., Carmichael, I.S.E., 1991. The compressibility of silicate liquids containing Fe_2O_3 and the effect of composition, temperature, oxygen fugacity and pressure on their redox states. Contributions to Mineralogy and Petrology 108, 82-92. doi:10.1007/BF00307328.

Labidi, J., Cartigny, P., Jackson, M.G., 2015. Multiple sulfur isotope composition of oxidized Samoan melts and the implications of a sulfur isotope 'mantle array' in chemical geodynamics. Earth and Planetary Science Letters 417, 28-39. doi:10.1016/j.epsl.2015.02.004.

Lesne, P., Kohn, S.C., Blundy, J., Witham, F., Botcharnikov, R.E., Behrens, H., 2011. Experimental simulation of closed-system degassing in the system basalt–H_2O–CO_2–S–Cl. Journal of Petrology 52, 1737-1762. doi:10.1093/petrology/egr027.

Longpré, M.-A., Klügel, A., Diehl, A., Stix, J., 2014. Mixing in mantle magma reservoirs prior to and during the 2011–2012 eruption at El Hierro, Canary Islands. Geology 42, 315-318. doi:10.1130/g35165.1.

Marini, L., Moretti, R., Accornero, M., 2011. Sulfur isotopes in magmatic-hydrothermal systems, melts, and magmas. Reviews in Mineralogy and Geochemistry 73, 423-492. doi:10.2138/rmg.2011.73.14.

Martí, J., Castro, A., Rodríguez, C., Costa, F., Carrasquilla, S., Pedreira, R., Bolos, X., 2013. Correlation of magma evolution and geophysical monitoring during the 2011–2012 El Hierro (Canary Islands) submarine eruption. Journal of Petrology 54, 1349-1373. doi:10.1093/petrology/egt014.

McDonough, W.F., Sun, S.-s., 1995. The composition of the Earth. Chemical Geology 120, 223-253. doi:10.1016/0009-2541(94)00140-4.

McKenzie, D., O'Nions, R.K., 1991. Partial melt distributions from inversion of rare earth element concentrations. Journal of Petrology 32, 1021-1091. doi:10.1093/petrology/32.5.1021.

Meletlidis, S., Di Roberto, A., Cerdeña, I.D., Pompilio, M., Bertagnini, A., Benito-Saz, M.A., Del Carlo, P., Aparicio, S.S.-M., 2015. New insight into the 2011-2012 unrest and eruption of El Hierro Island (Canary Islands) based on integrated geophysical, geodetical and petrological data. Annals of Geophysics 58, S0546. doi:10.4401/ag-6754.

Melián, G., Hernández, P.A., Padrón, E., Pérez, N.M., Barrancos, J., Padilla, G., Dionis, S., Rodríguez, F., Calvo, D., Nolasco, D., 2014. Spatial and temporal variations of diffuse CO_2 degassing at El Hierro volcanic system: Relation to the 2011–2012 submarine eruption. Journal of Geophysical Research: Solid Earth 119, 2014JB011013. doi:10.1002/2014JB011013.

Métrich, N., Berry, A.J., O'Neill, H.S.C., Susini, J., 2009. The oxidation state of sulfur in synthetic and natural glasses determined by X-ray absorption spectroscopy. Geochimica et Cosmochimica Acta 73, 2382-2399. doi:10.1016/j.gca.2009.01.025.

Métrich, N., Clocchiatti, R., 1996. Sulfur abundance and its speciation in oxidized alkaline melts. Geochimica et Cosmochimica Acta 60, 4151-4160. doi:10.1016/S0016-7037(96)00229-3.

Métrich, N., Wallace, P., 2008. Volatile abundances in basaltic magmas and their degassing paths tracked by melt inclusions. Reviews in Mineralogy and Geochemistry 69, 363-402. doi:10.2138/rmg.2008.69.10.

Michael, P., 1995. Regionally distinctive sources of depleted MORB: evidence from trace elements and H_2O. Earth and Planetary Science Letters 131, 301-320. doi:10.1016/0012-821X(95)00023-6.

Moore, L., Gazel, E., Tuohy, R., Lloyd, A., Esposito, R., Steele-MacInnis, M., Hauri, E.H., Wallace, P.J., Plank, T., Bodnar, R.J., 2015. Bubbles matter: An assessment of the contribution of vapor bubbles to melt inclusion volatile budgets. American Mineralogist 100, 806-823. doi:10.2138/am-2015-5036.

738 Moussallam, Y., Oppenheimer, C., Scaillet, B., Gaillard, F., Kyle, P., Peters, N., Hartley, M., Berlo, K., Donovan,
739 A., 2014. Tracking the changing oxidation state of Erebus magmas, from mantle to surface, driven by magma
740 ascent and degassing. Earth and Planetary Science Letters 393, 200-209. doi:10.1016/j.epsl.2014.02.055.

741 Neave, D.A., Maclennan, J., Edmonds, M., Thordarson, T., 2014. Melt mixing causes negative correlation of
742 trace element enrichment and CO_2 content prior to an Icelandic eruption. Earth and Planetary Science Letters
743 400, 272-283. doi:10.1016/j.epsl.2014.05.050.

744 Neave, D.A., Maclennan, J., Thordarson, T., Hartley, M.E., 2015. The evolution and storage of primitive melts in
745 the Eastern Volcanic Zone of Iceland: the 10 ka Grímsvötn tephra series (i.e. the Saksunarvatn ash).
746 Contributions to Mineralogy and Petrology 170, 1-23. doi:10.1007/s00410-015-1170-3.

747 Newman, S., Lowenstern, J.B., 2002. VolatileCalc: a silicate melt-H_2O-CO_2 solution model written in Visual Basic
748 for excel. Computers & Geosciences 28, 597-604. doi:10.1016/S0098-3004(01)00081-4.

749 Oppenheimer, C., Moretti, R., Kyle, P.R., Eschenbacher, A., Lowenstern, J.B., Hervig, R.L., Dunbar, N.W., 2011.
750 Mantle to surface degassing of alkalic magmas at Erebus volcano, Antarctica. Earth and Planetary Science
751 Letters 306, 261-271. doi:10.1016/j.epsl.2011.04.005.

752 Paonita, A., Martelli, M., 2006. Magma dynamics at mid-ocean ridges by noble gas kinetic fractionation:
753 assessment of magmatic ascent rates. Earth and Planetary Science Letters 241, 138-158.
754 doi:10.1016/j.epsl.2005.10.018.

755 Papale, P., Moretti, R., Barbato, D., 2006. The compositional dependence of the saturation surface of H_2O+CO_2
756 fluids in silicate melts. Chemical Geology 229, 78-95. doi:10.1016/j.chemgeo.2006.01.013.

757 Parat, F., Holtz, F., Klügel, A., 2011. S-rich apatite-hosted glass inclusions in xenoliths from La Palma:
758 constraints on the volatile partitioning in evolved alkaline magmas. Contributions to Mineralogy and Petrology
759 162, 463-478. doi:10.1007/s00410-011-0606-7.

760 Prytulak, J., Elliott, T., 2007. TiO_2 enrichment in ocean island basalts. Earth and Planetary Science Letters 263,
761 388-403. doi:10.1016/j.epsl.2007.09.015.

762 Putirka, K.D., 2008. Thermometers and barometers for volcanic systems. Reviews in Mineralogy and
763 Geochemistry 69, 61-120. doi:10.2138/rmg.2008.69.3.

764 Rivera, J., Lastras, G., Canals, M., Acosta, J., Arrese, B., Hermida, N., Micallef, A., Tello, O., Amblas, D., 2013.
765 Construction of an oceanic island: Insights from the El Hierro (Canary Islands) 2011–2012 submarine volcanic
766 eruption. Geology 41, 355-358. doi:10.1130/g33863.1.

767 Rosenthal, A., Hauri, E.H., Hirschmann, M.M., 2015. Experimental determination of C, F, and H partitioning
768 between mantle minerals and carbonated basalt, CO_2/Ba and CO_2/Nb systematics of partial melting, and the
769 CO_2 contents of basaltic source regions. Earth and Planetary Science Letters 412, 77-87.
770 doi:10.1016/j.epsl.2014.11.044.

771 Rowe, M.C., Kent, A.J.R., Nielsen, R.L., 2007. Determination of sulfur speciation and oxidation state of olivine
772 hosted melt inclusions. Chemical Geology 236, 303-322. doi:10.1016/j.chemgeo.2006.10.007.

773 Saal, A.E., Hauri, E.H., Langmuir, C.H., Perfit, M.R., 2002. Vapour undersaturation in primitive mid-ocean-ridge
774 basalt and the volatile content of Earth's upper mantle. Nature 419, 451-455. doi:10.1038/nature01073.

775 Santana-Casiano, J.M., González-Dávila, M., Fraile-Nuez, E., de Armas, D., González, A.G., Domínguez-Yanes,
776 J.F., Escánez, J., 2013. The natural ocean acidification and fertilization event caused by the submarine eruption
777 of El Hierro. Scientific Reports 3, 1140. doi:10.1038/srep01140.

778 Shaw, A., Hauri, E., Fischer, T., Hilton, D., Kelley, K., 2008. Hydrogen isotopes in Mariana arc melt inclusions:
779 Implications for subduction dehydration and the deep-Earth water cycle. Earth and Planetary Science Letters
780 275, 138-145. doi:10.1016/j.epsl.2008.08.015.

781 Shinohara, H., 2013. Volatile flux from subduction zone volcanoes: Insights from a detailed evaluation of the
782 fluxes from volcanoes in Japan. Journal of Volcanology and Geothermal Research 268, 46-63.
783 doi:10.1016/j.jvolgeores.2013.10.007.

784 Shishkina, T.A., Botcharnikov, R.E., Holtz, F., Almeev, R.R., Jazwa, A.M., Jakubiak, A.A., 2014. Compositional
785 and pressure effects on the solubility of H_2O and CO_2 in mafic melts. Chemical Geology 388, 112-129.
786 doi:10.1016/j.chemgeo.2014.09.001.

787 Sides, I.R., Edmonds, M., Maclennan, J., Swanson, D.A., Houghton, B.F., 2014. Eruption style at Kilauea
788 Volcano in Hawai'i linked to primary melt composition. Nature Geoscience 7, 464-469. doi:10.1038/ngeo2140.

789 Sigmarsson, O., Carn, S., Carracedo, J.C., 1998. Systematics of U-series nuclides in primitive lavas from the
790 1730–36 eruption on Lanzarote, Canary Islands, and implications for the role of garnet pyroxenites during
791 oceanic basalt formations. Earth and Planetary Science Letters 162, 137-151. doi:10.1016/S0012-
792 821X(98)00162-9.

793 Spilliaert, N., Allard, P., Métrich, N., Sobolev, A.V., 2006. Melt inclusion record of the conditions of ascent,
794 degassing, and extrusion of volatile-rich alkali basalt during the powerful 2002 flank eruption of Mount Etna
795 (Italy). Journal of Geophysical Research 111, B04203. doi:10.1029/2005jb003934.

796 Troll, V.R., Klügel, A., Longpré, M.-A., Burchardt, S., Deegan, F.M., Carracedo, J.C., Wiesmaier, S., Kueppers,
797 U., Dahren, B., Blythe, L.S., Hansteen, T.H., Freda, C., Budd, D.A., Jolis, E.M., Jonsson, E., Meade, F.C.,
798 Harris, C., Berg, S.E., Mancini, L., Polacci, M., Pedroza, K., 2012. Floating stones off El Hierro, Canary Islands:
799 xenoliths of pre-island sedimentary origin in the early products of the October 2011 eruption. Solid Earth 3, 97-
800 110. doi:10.5194/se-3-97-2012.

801 Wallace, P., 1998. Pre-eruptive H_2O and CO_2 contents of mafic magmas from the submarine to emergent shield
802 stages of Gran Canaria, in: Weaver, P.P.E., Schmincke, H.-U., Firth, J.V., Duffield, W. (Eds.), Proceedings of the
803 Ocean Drilling Program. Scientific results. Ocean Drilling Program, College Station, TX, pp. 411-420.

804 Wallace, P., Carmichael, I.S.E., 1994. S speciation in submarine basaltic glasses as determined by
805 measurements of S*Kα* X-ray wavelength shifts. American Mineralogist 79, 161-167.

806 Wallace, P.J., Edmonds, M., 2011. The sulfur budget in magmas: evidence from melt inclusions, submarine
807 glasses, and volcanic gas emissions. Reviews in Mineralogy and Geochemistry 73, 215-246.
808 doi:10.2138/rmg.2011.73.8.

809 Workman, R.K., Hart, S.R., 2005. Major and trace element composition of the depleted MORB mantle (DMM).
810 Earth and Planetary Science Letters 231, 53-72. doi:10.1016/j.epsl.2004.12.005.

811

812

Figure

Click here to download Figure: Fig_1_Map_revised_low.pdf

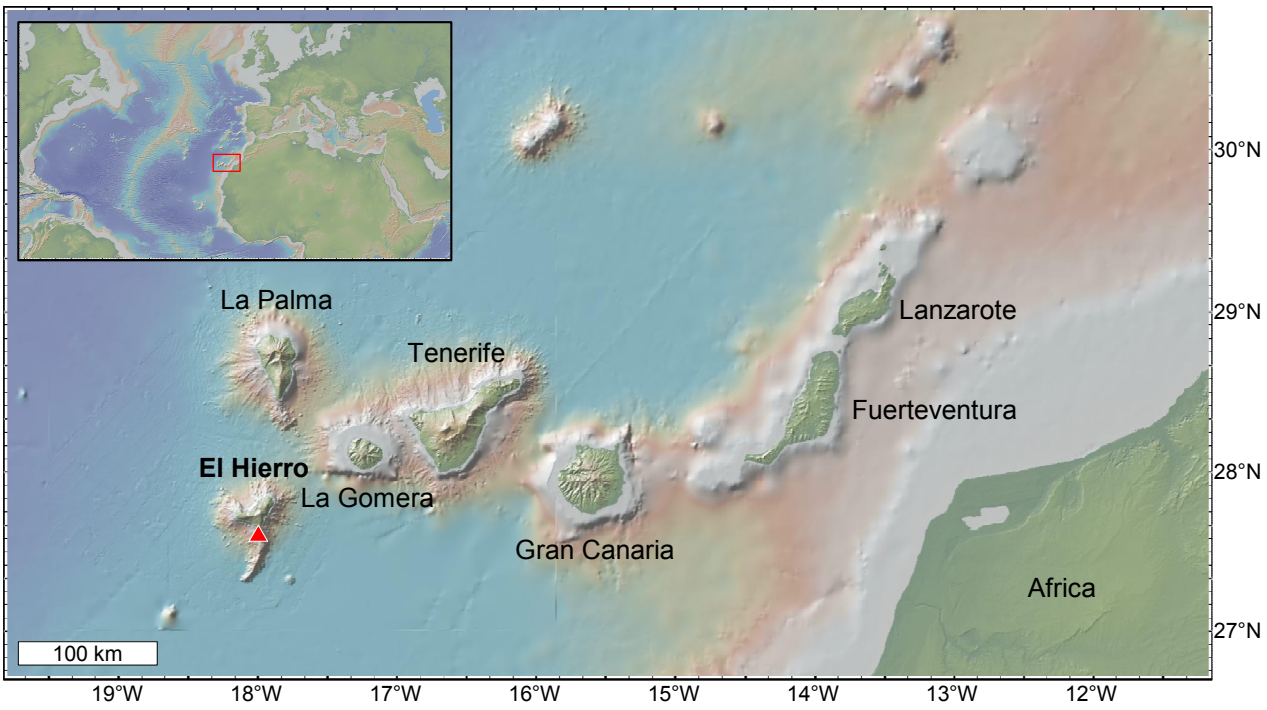

Figure 1

Figure
Click here to download Figure: Fig_2_Petrography_revised_low.pdf

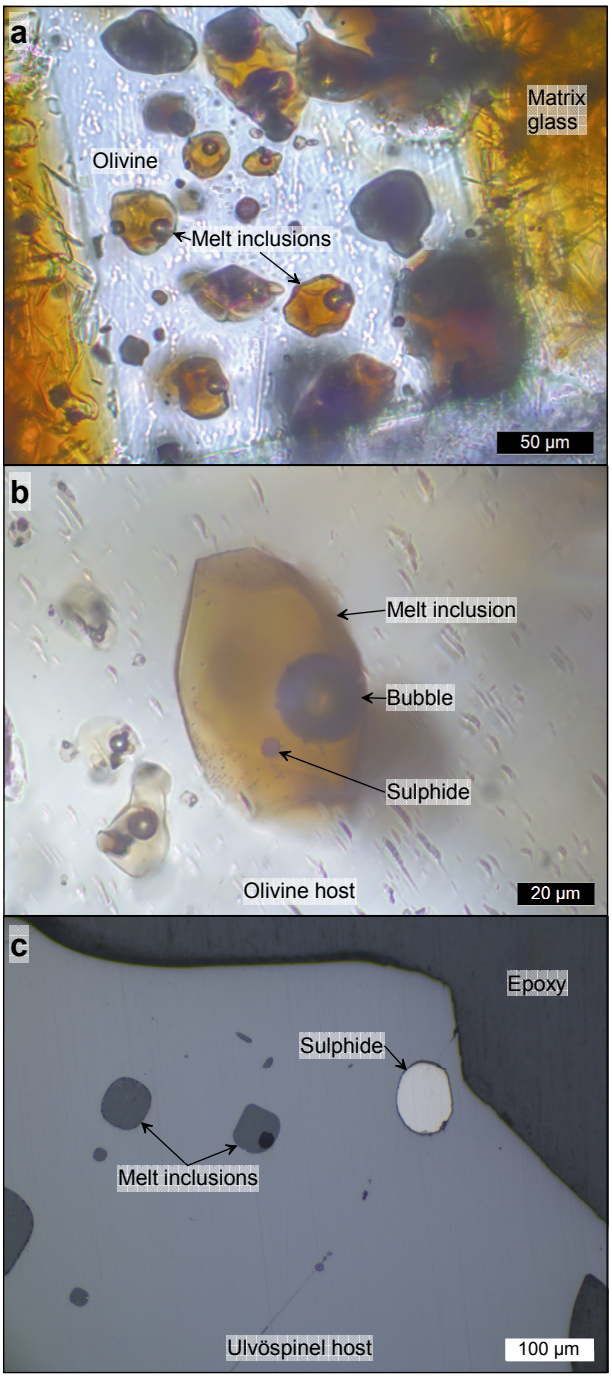

Figure 2

Figure

Click here to download Figure: Fig_3_Traces_revised_low.pdf

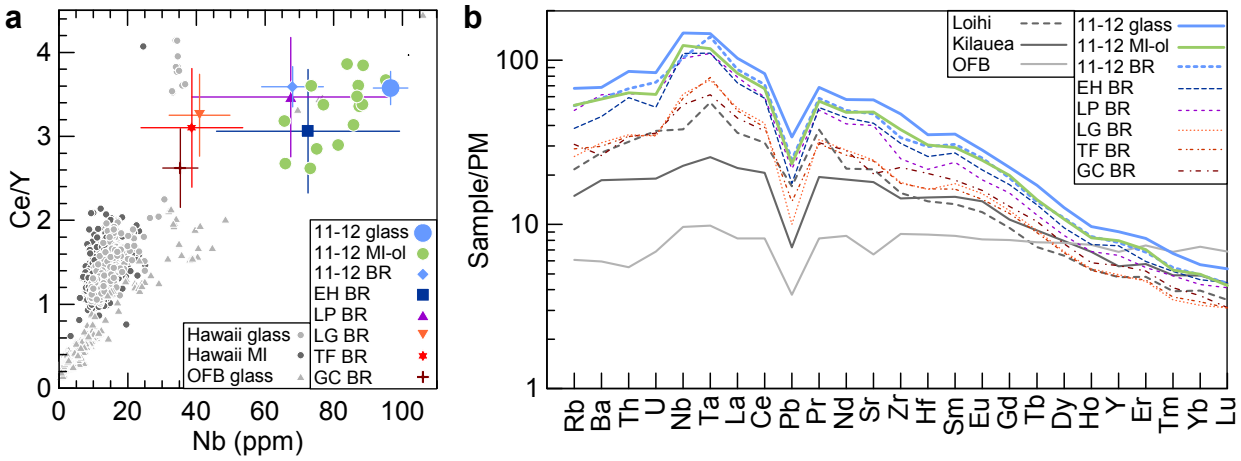

Figure 3

Figure
Click here to download Figure: Fig_4_CO2-H2O_revised_low.pdf

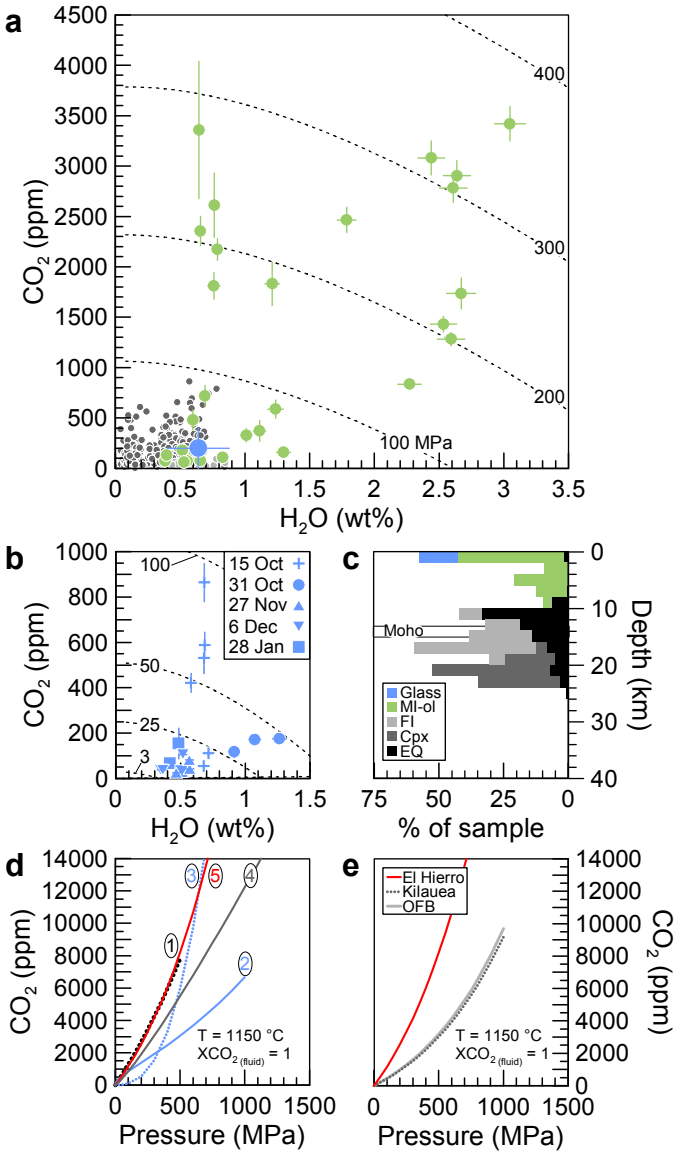

Figure 4

Figure
Click here to download Figure: Fig_5_Sulfur_revised_low.pdf

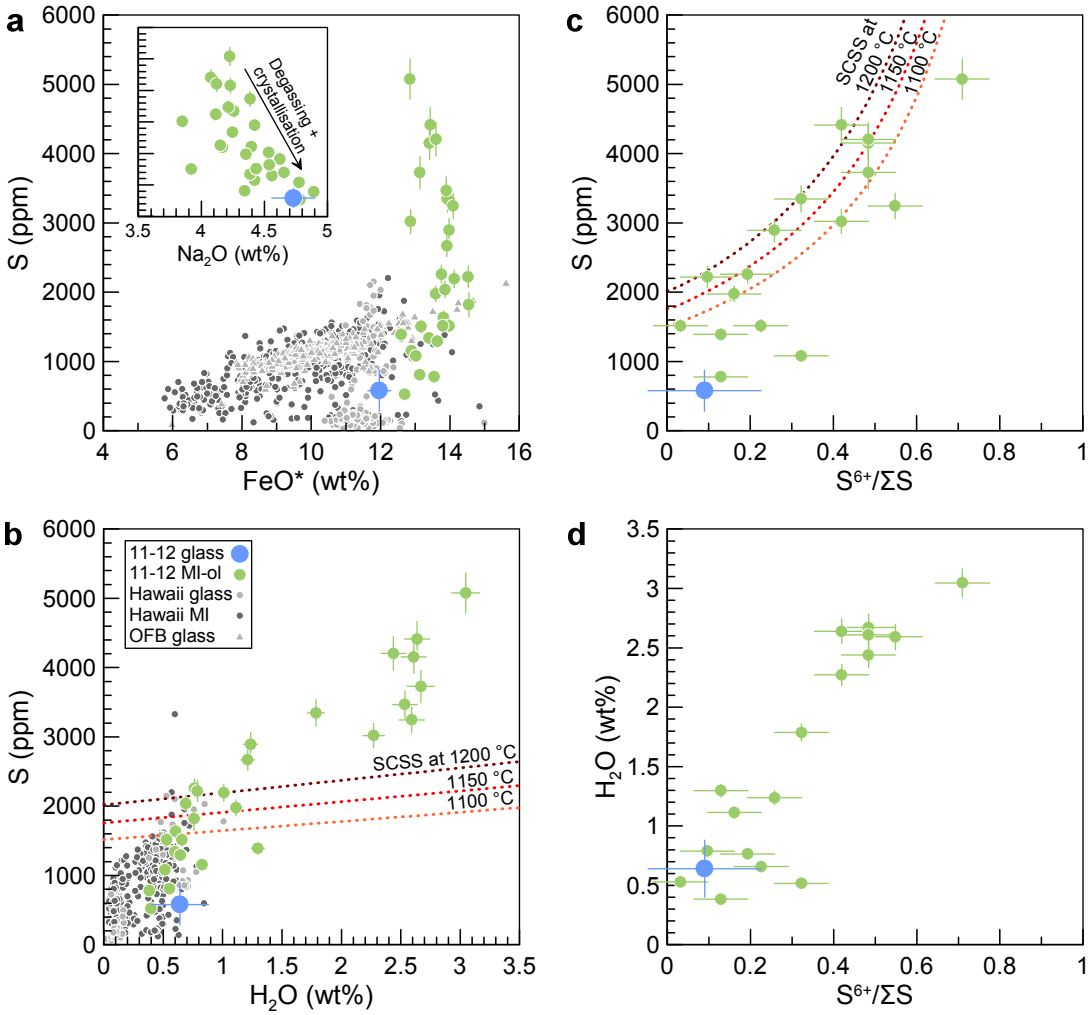

Figure 5

Figure

Click here to download Figure: Fig_6_Cl-F_revised_low.pdf

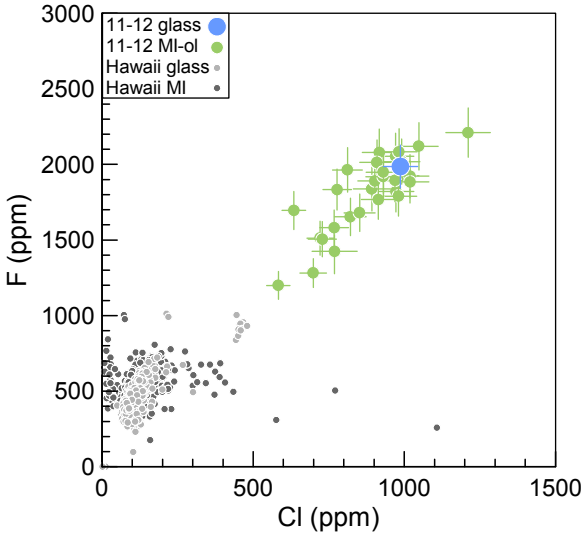

Figure 6

Figure
Click here to download Figure: Fig_7_Vol-Litho_Ratios_revised_low.pdf

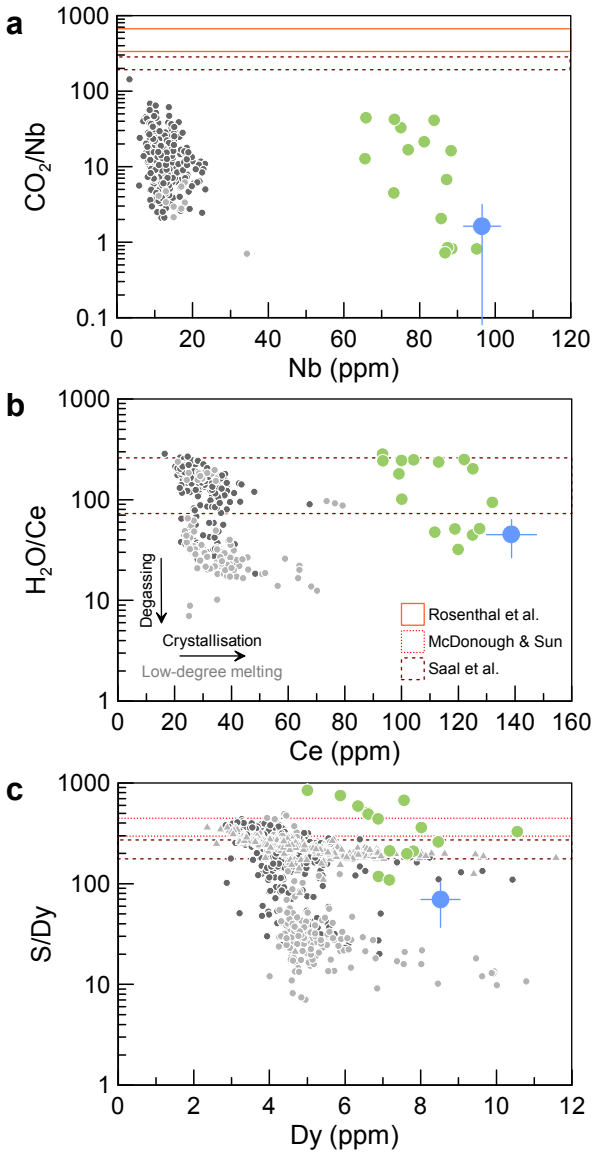

Figure 7

Figure

Click here to download Figure: Fig_8_S_Scenarios_revised_low.pdf

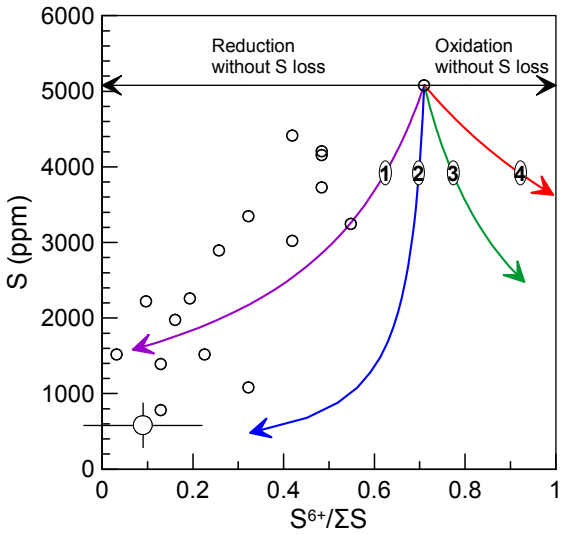

Figure 8

Figure

Click here to download Figure: Fig_9_D-Compress_Models_revised_low.pdf

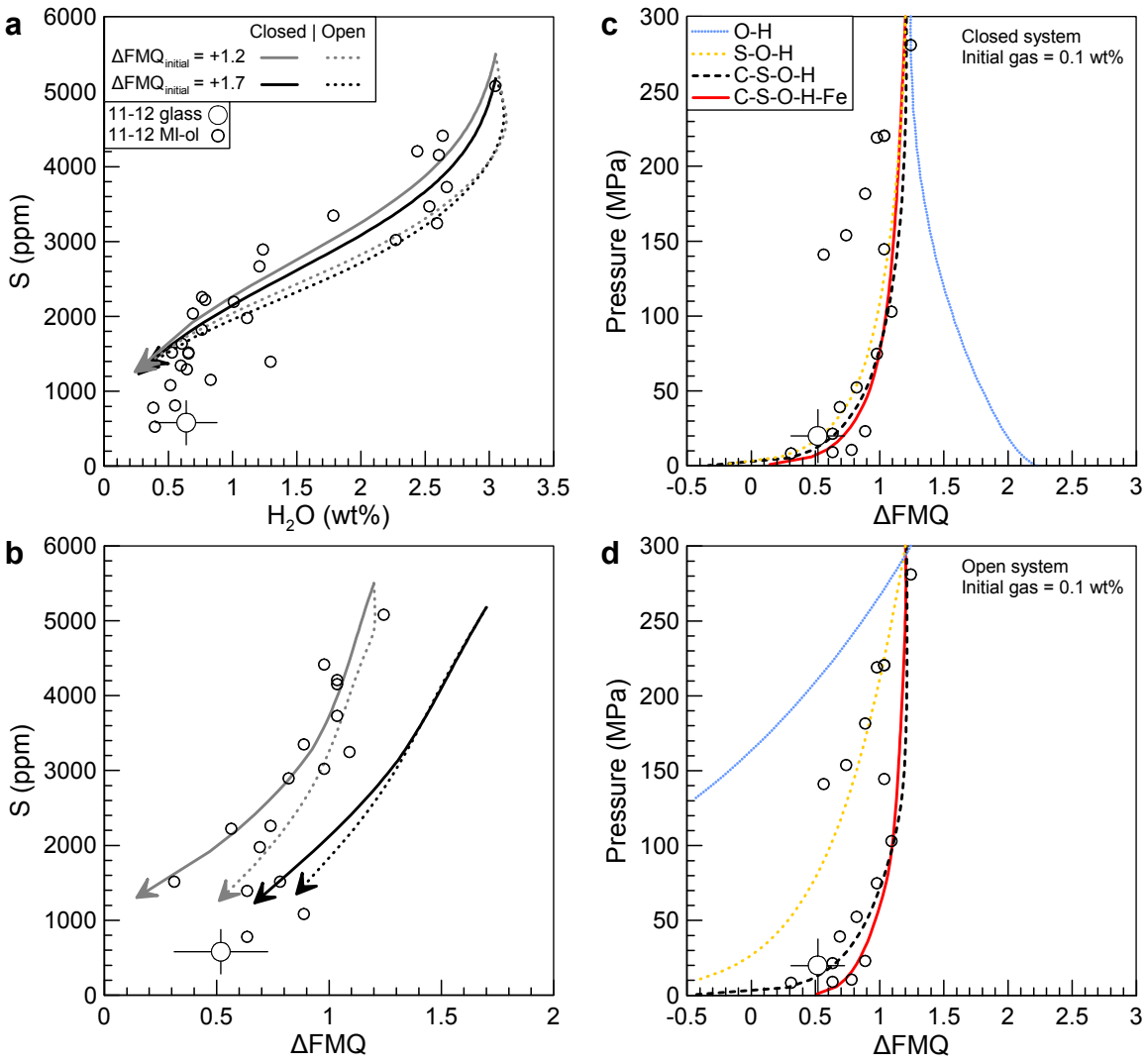

Figure 9

Figure

Click here to download Figure: Fig_10_Batch_Melting_revised_low.pdf

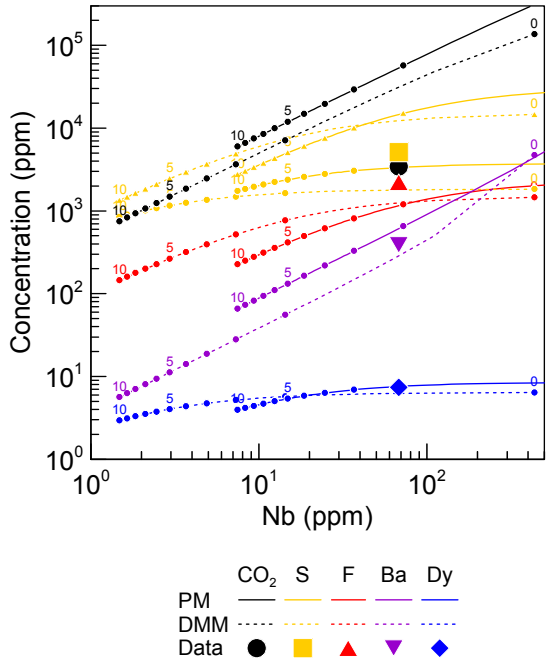

Figure 10